INTERNATIONAL JOURNAL FOR NUMERICAL METHODS IN FLUIDS
Int. J. Numer. Meth. Fluids 2009; **61**:311–340
Published online 17 November 2008 in Wiley InterScience (www.interscience.wiley.com). DOI: 10.1002/fld.1959

Large-eddy simulation of compressible flows using a spectral multidomain method

K. Sengupta[1], G. B. Jacobs[2] and F. Mashayek[1,*,†]

[1]*Department of Mechanical and Industrial Engineering, University of Illinois at Chicago, 842 West Taylor, Chicago, IL 60607, U.S.A.*
[2]*Department of Aerospace Engineering, San Diego State University, 5500 Campanile Drive, San Diego, CA 92182, U.S.A.*

SUMMARY

This paper discusses the development of a high-order, multidomain-based large-eddy simulation (LES) methodology for compressible flows. The LES model equations are approximated on unstructured grids of non-overlapping hexahedral sub-domains providing geometric flexibility. In each domain a high-order Chebyshev polynomial approximation represents the solution ensuring a highly accurate approximation with little numerical dispersion and diffusion. The sub-grid scale stress in the filtered LES equations is modeled with a dynamic eddy-viscosity model, while the heat flux is represented with an eddy diffusivity model, employing a turbulent Prandtl number. The model constants are evaluated through a flexible dynamic procedure that uses a high-order domain level filtering for the discrete test filter. The LES methodology is tested in a decaying isotropic turbulence and a channel flow. The LES method improves the resolution of the turbulence spectrum as compared with a direct numerical simulation (DNS) with the same method at the same grid resolution. The averaged and second-order statistics for LES computations are in close agreement with published results and resolved DNS. The high-order LES methodology requires fewer degrees of freedom as compared with lower-order LES methodologies to accurately resolve the turbulent flows. Copyright © 2008 John Wiley & Sons, Ltd.

Received 31 March 2008; Revised 23 July 2008; Accepted 2 October 2008

KEY WORDS: large-eddy simulation; multidomain method; compressible flow; spectral element filtering; isotropic turbulence; channel flow; collocation; turbulent flow; turbulence models; validation

1. INTRODUCTION

Large-eddy simulation (LES) has proven to be a viable technique for the computation of unsteady turbulent flows with large coherent structures in real complex applications. At moderate Reynolds

*Correspondence to: F. Mashayek, Department of Mechanical and Industrial Engineering, University of Illinois at Chicago, 842 West Taylor, Chicago, IL 60607, U.S.A.
†E-mail: mashayek@uic.edu

Contract/grant sponsor: U.S. Office of Naval Research

numbers, LES is more economical and/or accurate than other established computational techniques such as direct numerical simulation (DNS) and Reynolds-averaged Navier–Stokes (RANS) methods. DNS solves the governing equations without any turbulence modeling. Though it is accurate, DNS requires excessive computational cost to resolve the increasing turbulence scale range with increasing geometric complexity and Reynolds number. In RANS, on the other hand, all unsteady turbulence scales are modeled. While this reduces computational cost and enables the computation of most engineering applications, it also prevents RANS from adequately capturing the true dynamics of the flow. LES bridges the gap between DNS and RANS and efficiently computes unsteady turbulent flows in moderately complex geometries at midrange Reynolds numbers found in many real applications. LES is based on scale separation in turbulent flows. The large scales, which are anisotropic and sensitive to boundary conditions, are computed directly as in DNS, while the small scales that are more isotropic and universal are modeled. The modeling of the small scales reduces the computational cost, while the computation of the large scales provides detailed flow field information.

Numerical schemes are crucially affecting the fidelity of LES. Numerical errors in space and time can smear the solutions, overly dissipate turbulence, and thus lead to an inaccurate computation of the turbulent flow. Ghosal [1] performed an analysis of the effect of numerical errors of a finite difference method on LES. He found that for low-order finite difference schemes, the truncation error may be larger than modeled sub-grid stresses, unless the filter width is significantly larger than the grid size. Kravchenko and Moin [2] later extended the analysis to include the role of aliasing errors. It was shown that for low-order finite differences, the high-wavenumber part of the energy spectrum is heavily distorted by truncation errors and the contribution from the sub-grid model becomes small. In addition, low-order schemes have large dispersion errors, which reduce the temporal accuracy of unsteady (wave-dominated) flow computations.

With a high-order scheme, many of the numerical error-related inaccuracies of lower-order schemes can be reduced and fewer degrees of freedom are required for an accurate solution. However, combining high-order accuracy with other desirable properties of an LES method including geometric flexibility and conservation properties has proven to be challenging. Conservative, low-order finite volume [3, 4] and finite element [5] methods have been developed, which allow for complex geometry computation, but the geometric flexibility of the current high-order LES, which mostly relies on spectral and compact finite difference methods [6], is limited. Single domain spectral methods based on, for example, Fourier series approximations have desirable high-wavenumber characteristics, but can only be used for rectangular geometries. Compact finite difference methods are more versatile than the single domain spectral schemes. However, the block Cartesian mesh requirement and overlapping stencil of compact difference methods complicate both boundary condition implementation and an accurate, robust, parallel implementation for complex geometries. Another drawback of the high accuracy of both spectral and high-order finite difference methods is that aliasing errors affect the stability of the methods. Aliasing errors can be reduced by a modified form of the non-linear advection terms [7] or by using non-conservative form of the energy equation [8]. Unfortunately, these modifications do not guarantee robustness especially at high Mach numbers.

Spectral element methods [9, 10] are excellent candidates for LES since they combine the accuracy of single domain spectral schemes with the flexibility of finite element method. In spectral elements the spatial resolution can be conveniently altered either by increasing the number of elements (h-refinement) or by increasing the polynomial order within the elements (p-refinement). In smooth solution spaces, the method provides asymptotically exponential rate of spatial

DOI: 10.1002/fld

convergence with p-refinement. Low dispersion errors in these methods lead to high temporal accuracy, making them suitable for wave-dominated, unsteady problems. Moreover, low degree of data connectivity between non-overlapping elements facilitates efficient boundary condition application and parallel implementation.

Though spectral/hp element-based DNS computations are well established, there have been limited attempts to perform spectral element-based LES. Spectral element filtering strategies for LES were studied by Blackburn and Schmidt [11]. They investigated three different filtering techniques within two-dimensional spectral elements for the simulation of incompressible turbulent channel flow with a dynamic sub-grid model. Fischer and Mullen [12] introduced a spectral element filtering technique to stabilize their DNS. Levin *et al*. [13] applied a two-step filtering procedure to control the growth of non-linear instabilities in their eddy resolving spectral element ocean model. A combined spectral element-Fourier method was used by Karamanos [14] for LES with an explicit sub-grid model. Karamanos and Karniadakis [15] introduced spectral vanishing viscosity concept for LES. The implementation was tested for turbulent channel flow using Fourier discretization in the streamwise direction and spectral/hp quadrilateral elements in the cross flow and wall-normal directions. These studies have focused on LES of *incompressible* flows. To the best of the authors' knowledge there has not been any published work on LES of *compressible* flows using spectral element method.

In this paper, we develop a spectral/hp element LES technique for compressible flows using a Chebyshev spectral multidomain method [16–18]. The method combines many features that are desirable in a numerical methodology for LES of turbulent flows in complex geometries, including: a high-order approximation within each sub-domain, which restricts the numerical errors; complex geometries are easily computed with the unstructured hexahedral grid; the method is robust; the flux-based methodology leads to a conservative scheme; and the non-overlapping elements yield perfect parallelization implementation as well as easy boundary condition implementation. We model the sub-grid scales using an eddy-viscosity model. A flexible dynamic procedure is employed to evaluate the sub-grid model constants. The explicit filtering associated with the dynamic procedure is accomplished through a sub-domain-based high-order Lagrange-interpolant-projection procedure consistent with the high-order multidomain method. The characteristics of the LES methodology are tested in a decaying isotropic turbulence and a turbulent channel flow.

This paper is organized as follows. First, we describe the governing equations for compressible flows and present the numerical method. Then, we discuss the LES formulation including the filtered equations, the sub-grid models, and the dynamic procedure. Next, we test our methodology in an isotropic turbulence and a turbulent channel flow. Conclusions and recommendations are reserved for the final section.

2. GOVERNING EQUATIONS AND NUMERICAL FORMULATION

2.1. Compressible Navier–Stokes equations

The governing equations for the compressible and viscous fluid flow are the conservation statements for mass, momentum, and energy. They are presented in non-dimensional, conservative form with Cartesian tensor notation:

$$\frac{\partial \rho}{\partial t} + \frac{\partial (\rho u_j)}{\partial x_j} = 0 \tag{1}$$

DOI: 10.1002/fld

$$\frac{\partial(\rho u_i)}{\partial t}+\frac{\partial(\rho u_i u_j+p\delta_{ij})}{\partial x_j}=\frac{\partial \sigma_{ij}}{\partial x_j} \tag{2}$$

$$\frac{\partial(\rho e)}{\partial t}+\frac{\partial[(\rho e+p)u_j]}{\partial x_j}=-\frac{\partial q_j}{\partial x_j}+\frac{\partial(\sigma_{ij}u_i)}{\partial x_j} \tag{3}$$

The total energy, viscous stress tensor, and heat flux vector are, respectively, given as

$$\rho e=\frac{p}{\gamma-1}+\frac{1}{2}\rho u_k u_k \tag{4}$$

$$\sigma_{ij}=\frac{\mu}{Re_f}\left(\frac{\partial u_i}{\partial x_j}+\frac{\partial u_j}{\partial x_i}-\frac{2}{3}\frac{\partial u_k}{\partial x_k}\delta_{ij}\right) \tag{5}$$

$$q_j=-\frac{\mu}{(\gamma-1)Re_f Pr_f M_f^2}\frac{\partial T}{\partial x_j} \tag{6}$$

The reference Reynolds number Re_f is based on the reference density ρ_f^*, velocity U_f^*, length L_f^*, and molecular viscosity μ_f^* and is given by $Re_f=\rho_f^* U_f^* L_f^*/\mu_f^*$. $Pr_f=\mu_f^* C_p/k^*$ is the reference Prandtl number. The superscript $*$ denotes dimensional quantities. The above equation set is closed by the equation of state

$$p=\frac{\rho T}{\gamma M_f^2} \tag{7}$$

where M_f is the reference Mach number, taken to be 1 in this work. The conservation equations can be cast in the matrix form:

$$\frac{\partial \mathbf{Q}}{\partial t}+\frac{\partial \mathbf{F}_i^{\mathrm{a}}}{\partial x_i}-\frac{\partial \mathbf{F}_i^{\mathrm{v}}}{\partial x_i}=0 \tag{8}$$

where

$$\mathbf{Q}=\begin{pmatrix}\rho\\ \rho u_1\\ \rho u_2\\ \rho u_3\\ \rho e\end{pmatrix} \tag{9}$$

$$\mathbf{F}_i^{\mathrm{a}}=\begin{pmatrix}\rho u_i\\ \rho u_1 u_i+p\delta_{i1}\\ \rho u_2 u_i+p\delta_{i2}\\ \rho u_3 u_i+p\delta_{i3}\\ (\rho e+p)u_i\end{pmatrix} \tag{10}$$

DOI: 10.1002/fld

$$\mathbf{F}_i^{\mathrm{v}} = \begin{pmatrix} 0 \\ \sigma_{i1} \\ \sigma_{i2} \\ \sigma_{i3} \\ -q_i + u_k \sigma_{ik} \end{pmatrix} \tag{11}$$

Here $\mathbf{Q}$ is the vector of the conserved variables, while $\mathbf{F}_i^{\mathrm{a}}$ and $\mathbf{F}_i^{\mathrm{v}}$ are the advective and viscous flux vectors, respectively, in the x_i direction.

2.2. Numerical methodology

This section briefly describes the staggered-grid Chebyshev multidomain method. For a more complete description of the method, see [16, 18]. In this method, the computational domain, Ω, is divided into non-overlapping hexahedral sub-domains, D_k:

$$\Omega = \sum D_k \tag{12}$$

The sub-domains are mapped onto a unit hexahedron $D_k \leftrightarrow [0,1]\times[0,1]\times[0,1]$ by an isoparametric mapping [19]. Isoparametric mapping ensures that the spectral accuracy of the scheme is not affected by the domain boundary approximation. The staggered-grid method uses two sets of grids, one for the solution (Chebyshev–Gauss grid) and another for the computation of the fluxes (Chebyshev–Gauss–Lobatto grids). In one space dimension the Gauss and Gauss–Lobatto quadrature points are defined by

$$X_{j+1/2} = \frac{1}{2}\left\{1 - \cos\left[\frac{(2j+1)\pi}{2N}\right]\right\}, \quad j = 0, \ldots, N-1 \tag{13}$$

and

$$X_j = \frac{1}{2}\left\{1 - \cos\left[\frac{\pi j}{N}\right]\right\}, \quad j = 0, \ldots, N \tag{14}$$

respectively, on the unit interval [0, 1]. The Gauss grid in three dimensions, henceforth referred to as the ggg grid, is the tensor product of the one-dimensional grid defined in Equation (13). The solution vector, $\tilde{\mathbf{Q}}$, where the tilde denotes mapped space, is approximated on the ggg grid as

$$\tilde{\mathbf{Q}}^{\mathrm{ggg}}(X,Y,Z) = \sum_{i=0}^{N-1}\sum_{j=0}^{N-1}\sum_{k=0}^{N-1} \tilde{\mathbf{Q}}^{\mathrm{ggg}}_{i+1/2,j+1/2,k+1/2} h_{i+1/2}(X) h_{j+1/2}(Y) h_{k+1/2}(Z) \tag{15}$$

where $N-1$ is the approximation order. Here $h_{i+1/2} \in \mathbf{P}_{N-1}$ is the Lagrange interpolating polynomial defined on the Gauss grid:

$$h_{i+1/2}(\xi) = \prod_{m=0, m\neq i}^{N-1} \left(\frac{\xi - X_{m+1/2}}{X_{i+1/2} - X_{m+1/2}}\right) \tag{16}$$

The fluxes in each direction $\mathbf{F}_i$ are defined on the Gauss–Lobatto grids shown in Figure 1. The x-direction flux ($\mathbf{F}_1$) is evaluated at the Lobatto–Gauss–Gauss grid (lgg) denoted by open squares, $(X_i, Y_{j+1/2}, Z_{k+1/2})$, $i = 0, 1, \ldots, N$, $j, k = 0, 1, \ldots, N-1$, the y-direction flux ($\mathbf{F}_2$) at the

DOI: 10.1002/fld

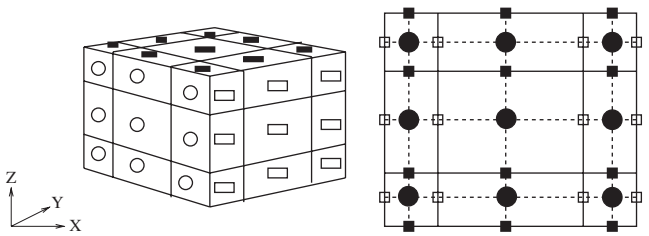

Figure 1. Staggered arrangement of solution variable and fluxes: closed circles—ggg points, open squares—lgg points, open circles—glg points, closed squares—ggl points.

Gauss–Lobatto–Gauss grid (glg) denoted by open circles, $(X_{i+1/2}, Y_j, Z_{k+1/2})$, $j=0,1,\ldots,N$, $i,k=0,1,\ldots,N-1$, and the z-direction flux ($\mathbf{F}_3$) at the Gauss–Gauss–Lobatto grid (ggl) denoted by closed squares, $(X_{i+1/2}, Y_{j+1/2}, Z_k)$, $k=0,1,\ldots,N$, $i,j=0,1,\ldots,N-1$. The flux vectors are computed by reconstructing the solution at the Lobatto points through interpolations using polynomials of the type in Equation (15). The interpolation operation is given as

$$\mathbf{Q}^{\mathrm{lgg}}(X_i, Y_{j+1/2}, Z_{k+1/2}) = \sum_{m=0}^{N-1}\sum_{n=0}^{N-1}\sum_{p=0}^{N-1} \frac{\tilde{\mathbf{Q}}^{\mathrm{ggg}}_{m+1/2,n+1/2,p+1/2}}{J_{m+1/2,n+1/2,p+1/2}} h_{m+1/2}(X_i) \times h_{n+1/2}(Y_{j+1/2}) h_{p+1/2}(Z_{k+1/2}) \tag{17}$$

in the x direction, which reduces to a one-dimensional operation

$$\mathbf{Q}^{\mathrm{lgg}}(X_i, Y_{j+1/2}, Z_{k+1/2}) = \sum_{m=0}^{N-1} \frac{\tilde{\mathbf{Q}}^{\mathrm{ggg}}_{m+1/2,j+1/2,k+1/2}}{J_{m+1/2,j+1/2,k+1/2}} h_{m+1/2}(X_i) \tag{18}$$

due to the cardinal property of the Lagrange interpolating polynomial. Similarly for the y and z directions the interpolants are given by

$$\mathbf{Q}^{\mathrm{glg}}(X_{i+1/2}, Y_j, Z_{k+1/2}) = \sum_{n=0}^{N-1} \frac{\tilde{\mathbf{Q}}^{\mathrm{ggg}}_{i+1/2,n+1/2,k+1/2}}{J_{i+1/2,n+1/2,k+1/2}} h_{n+1/2}(Y_j) \tag{19}$$

$$\mathbf{Q}^{\mathrm{ggl}}(X_{i+1/2}, Y_{j+1/2}, Z_k) = \sum_{p=0}^{N-1} \frac{\tilde{\mathbf{Q}}^{\mathrm{ggg}}_{i+1/2,j+1/2,p+1/2}}{J_{i+1/2,j+1/2,p+1/2}} h_{p+1/2}(Z_k) \tag{20}$$

where J is the Jacobian of transformation from the physical space to the mapped space. Once the solution values are interpolated to the Lobatto grid, the advective fluxes are computed. The interface points will have different flux values due to discontinuity of solution values at the sub-domain boundaries. The patching of the advective fluxes is described later. The viscous fluxes are computed in two steps. The solution interpolant at the Lobatto grids must be continuous for a unique first derivative at the sub-domain interfaces. This is ensured by a Dirichlet patching or averaging of the solution on both sides of the interface. After the Lobatto interpolants for the solution values are patched, their derivatives are computed at the Gauss points. The gradients are then interpolated back to the Lobatto points. The viscous fluxes are computed using the functional relations (5) and (6). The interface condition for viscous fluxes and any Neumann boundary condition are applied at this point. Finally, the total flux is obtained by adding the inviscid and viscous parts. Once the

DOI: 10.1002/fld

total fluxes are computed at the lgg, glg, and ggl points, the flux interpolants are constructed as

$$\tilde{\mathbf{F}}_1(X,Y,Z)=\sum_{m=0}^{N}\sum_{n=0}^{N-1}\sum_{p=0}^{N-1}\tilde{\mathbf{F}}_{1m,n+1/2,p+1/2}l_m(X)h_{n+1/2}(Y)h_{p+1/2}(Z) \tag{21}$$

$$\tilde{\mathbf{F}}_2(X,Y,Z)=\sum_{m=0}^{N-1}\sum_{n=0}^{N}\sum_{p=0}^{N-1}\tilde{\mathbf{F}}_{2m+1/2,n,p+1/2}h_{m+1/2}(X)l_n(Y)h_{p+1/2}(Z) \tag{22}$$

$$\tilde{\mathbf{F}}_3(X,Y,Z)=\sum_{m=0}^{N-1}\sum_{n=0}^{N-1}\sum_{p=0}^{N}\tilde{\mathbf{F}}_{3m+1/2,n+1/2,p}h_{m+1/2}(X)h_{n+1/2}(Y)l_p(Z) \tag{23}$$

These fluxes are differentiated and evaluated at the ggg grid to give pointwise derivatives:

$$\frac{\partial\tilde{\mathbf{F}}_1(X_{i+1/2},Y_{j+1/2},Z_{k+1/2})}{\partial X}=\sum_{m=0}^{N}\tilde{\mathbf{F}}_1(X_m,Y_{j+1/2},Z_{k+1/2})\frac{\partial l_m(X_{i+1/2})}{\partial X} \tag{24}$$

$$\frac{\partial\tilde{\mathbf{F}}_2(X_{i+1/2},Y_{j+1/2},Z_{k+1/2})}{\partial Y}=\sum_{n=0}^{N}\tilde{\mathbf{F}}_2(X_{i+1/2},Y_n,Z_{k+1/2})\frac{\partial l_n(Y_{j+1/2})}{\partial Y} \tag{25}$$

$$\frac{\partial\tilde{\mathbf{F}}_3(X_{i+1/2},Y_{j+1/2},Z_{k+1/2})}{\partial Z}=\sum_{p=0}^{N}\tilde{\mathbf{F}}_3(X_{i+1/2},Y_{j+1/2},Z_p)\frac{\partial l_p(Z_{k+1/2})}{\partial Z} \tag{26}$$

Finally, the semi-discrete equation for the solution unknowns at the ggg grid is given by

$$\left[\frac{\mathrm{d}\tilde{\mathbf{Q}}}{\mathrm{d}t}\right]_{i+1/2,j+1/2,k+1/2}+\left[\frac{\partial\tilde{\mathbf{F}}_i}{\partial X_i}\right]_{i+1/2,j+1/2,k+1/2}=0 \tag{27}$$

which is advanced in time using a fourth-order low storage Runge–Kutta scheme.

2.3. Interface and boundary treatment

Interpolation of the solution by Equations (18)–(20) leads to different solution values at the sub-domain interface points, one from each of the contributing sub-domains. The solution is therefore discontinuous. The coupling between sub-domains is enforced by continuous advective and viscous fluxes at the interface points. Enforcing flux continuity yields a conservative method. The inviscid fluxes are computed using an approximate Riemann solver. Formally, given the two solution states $\mathbf{Q}_N^{k-1}$ and $\mathbf{Q}_0^k$ (the superscript denotes the sub-domain number and the subscript denotes the node number within a sub-domain), the flux in each spatial direction, with the assumption that waves are normal to the interface, can be expressed as

$$\Gamma^{\mathrm{a}}(\mathbf{Q}_N^{k-1},\mathbf{Q}_0^k)=\tfrac{1}{2}[\mathbf{F}^{\mathrm{a}}(\mathbf{Q}_N^{k-1})+\mathbf{F}^{\mathrm{a}}(\mathbf{Q}_0^k)]-\tfrac{1}{2}\mathbf{R}|\lambda|\mathbf{R}^{-1}(\mathbf{Q}_0^k-\mathbf{Q}_N^{k-1}) \tag{28}$$

where $\mathbf{F}^{\mathrm{a}}$ is the vector of advective fluxes. $\mathbf{R}$ is the matrix of the right eigenvectors of the Jacobian of $\mathbf{F}^{\mathrm{a}}$ computed using Roe-average of $\mathbf{Q}_N^{k-1}$ and $\mathbf{Q}_0^k$. For imposing inviscid boundary conditions, the physical boundary can be viewed as an interface between the external state and the computational domain. The Riemann solver is applied between the external specified flow solution and the internal solution vector. The above treatment of the advective fluxes is similar to that employed in

DOI: 10.1002/fld

discontinuous Galerkin methods (e.g. [20]). However, there is a subtle but important difference. Unlike the strong form of the discontinuous Galerkin formulation, where an explicit numerical flux appears in the boundary integral, the spectral multidomain method here does not involve any numerical flux. Also, the interface treatment here does not include any parameter to control the stability such as that used in the multidomain penalty method of Diamessis *et al*. [21]. The upwind approximate Riemann solver by Roe introduces dissipation at the sub-domain interfaces that is stabilizing.

The viscous fluxes are determined as outlined in the previous sub-section. Continuity of the viscous fluxes is established by averaging the viscous flux vector from both sides of the interface:

$$\Gamma_0^{\mathrm{v},k} = \Gamma_N^{\mathrm{v},k-1} = \tfrac{1}{2}(\mathbf{F}_0^{\mathrm{v},k} + \mathbf{F}_N^{\mathrm{v},k-1}) \tag{29}$$

The above treatment follows the work of Bassi and Rebay [22] and is also commonly used in discontinuous Galerkin methods for compressible flows [20, 23]. The Neumann boundary conditions are imposed at the boundary points at this stage.

3. LES FORMULATION

3.1. Filtered Navier–Stokes equations

The LES method presented here solves the filtered Navier–Stokes equations. By applying a spatial low-pass (in frequency domain) convolution filter to the Navier–Stokes equations, the turbulence scales are separated. The filter in physical space is represented by the following convolution product:

$$\bar{f}(\mathbf{x}, t) = \int_\Omega f(\mathbf{x}', t) G(\mathbf{x} - \mathbf{x}')\, \mathrm{d}\mathbf{x}' \tag{30}$$

where G is the filter kernel and Ω represents the flow domain. We apply the Favre, density weighted filtering operation, typical for LES of compressible turbulence:

$$\tilde{f} = \frac{\overline{\rho f}}{\bar{\rho}} \tag{31}$$

where overbar denotes the filtering operation.

Applying this filter yields the following filtered conservation equations:

$$\frac{\partial \bar{\rho}}{\partial t} + \frac{\partial (\bar{\rho} \widetilde{u_j})}{\partial x_j} = 0 \tag{32}$$

$$\frac{\partial (\bar{\rho} \widetilde{u_i})}{\partial t} + \frac{\partial (\bar{\rho} \widetilde{u_i} \widetilde{u_j} + \bar{p} \delta_{ij})}{\partial x_j} = \frac{\partial \tilde{\sigma}_{ij}}{\partial x_j} - \frac{\partial \tau_{ij}^{\mathrm{sgs}}}{\partial x_j} + \frac{\partial (\bar{\sigma}_{ij} - \tilde{\sigma}_{ij})}{\partial x_j} \tag{33}$$

$$\begin{aligned} \frac{\partial (\overline{\rho e})}{\partial t} + \frac{\partial [(\overline{\rho e} + \bar{p}) \tilde{u}_j]}{\partial x_j} = & -\frac{\partial \tilde{q}_j}{\partial x_j} + \frac{\partial (\tilde{\sigma}_{ij} \tilde{u}_i)}{\partial x_j} - \frac{1}{(\gamma - 1) M_f^2} \frac{\partial q_j^{\mathrm{sgs}}}{\partial x_j} + \frac{\partial (\bar{q}_j - \tilde{q}_j)}{\partial x_j} \\ & + \frac{\partial (\tilde{u}_j [\bar{\sigma}_{jk} - \tilde{\sigma}_{jk}])}{\partial x_k} + \frac{1}{2} \frac{\partial}{\partial x_j} \bar{\rho} (\widetilde{u_k u_k u_j} - \tilde{u}_k \tilde{u}_k \tilde{u}_j - \tau_{kk}^{\mathrm{sgs}} \tilde{u}_j) \end{aligned} \tag{34}$$

DOI: 10.1002/fld

The filtering leads to several terms in Equations (33) and (34) that require closure. τ_{ij}^{sgs} is the sub-grid scale stress tensor and q_j^{sgs} is the sub-grid turbulent heat flux. The sub-grid terms physically represent the effect of the unresolved (sub-grid) scales on the resolved scales. The second unclosed term in the filtered momentum equation is $(\bar{\sigma}_{ij}-\tilde{\sigma}_{ij})$, which results from Favre filtering of the viscous stresses. The filtered energy equation has three more unclosed terms in addition to the sub-grid heat flux: the term $\partial(\bar{q}_j-\tilde{q}_j)/\partial x_j$ that results from the Favre filtering of the diffusive heat flux; the term $\partial(\tilde{u}_j[\bar{\sigma}_{jk}-\tilde{\sigma}_{jk}])/\partial x_k$ that is analogous to the sub-grid scale viscous dissipation; and finally the divergence of turbulent diffusion, $\frac{1}{2}(\partial/\partial x_j)\bar{\rho}(\widetilde{u_k u_k u_j}-\tilde{u}_k\tilde{u}_k\tilde{u}_j-\tau_{kk}^{\text{sgs}}\tilde{u}_j)$. The modeling of the unclosed terms is discussed in Section 3.2.

3.2. Sub-grid scale model

The unclosed terms in the filtered equations require modeling. We first consider the modeling of the unclosed terms in the momentum equation (Equation (33)). The term $(\bar{\sigma}_{ij}-\tilde{\sigma}_{ij})$ is neglected following [24, 25]. The sub-grid term $\tau_{ij}^{\text{sgs}}=\bar{\rho}(\widetilde{u_i u_j}-\tilde{u}_i\tilde{u}_j)$ is modeled using the modification of the Germano model [26] for compressible flows (given by Moin *et al*. [8]). The expression for τ_{ij}^{sgs} is accordingly given as

$$\tau_{ij}^{\text{sgs}}=-2C_{\text{s}}\bar{\Delta}^2\bar{\rho}|\tilde{S}|(\tilde{S}_{ij}-\tfrac{1}{3}\tilde{S}_{mm}\delta_{ij})+\tfrac{1}{3}\tau_{kk}^{\text{sgs}}\delta_{ij} \tag{35}$$

The trace of the sub-grid stress tensor τ_{kk}^{sgs} cannot be included in the modified pressure in compressible flow, and thus has to be modeled separately. Different models of τ_{kk}^{sgs} have been proposed (see [27, 28]). However, the study by Squires [29] demonstrated that there is no difference in the LES results of compressible isotropic turbulence at low Mach number when τ_{kk}^{sgs} is neglected. Vreman *et al*. [30] confirmed the above findings with their simulation of three-dimensional compressible mixing layers at a mean convective Mach number of 0.2. In their *a priori* test, the sub-grid scale (SGS) model that neglects τ_{kk}^{sgs} was found to be in better agreement with DNS results. Moreover, simulations conducted with a dynamic model for τ_{kk}^{sgs} were often unstable for the cases studied by Vreman *et al*. [30]. Therefore, in LES of low Mach number flow, neglecting the trace of sub-grid stress tensor will not introduce large errors. We will therefore neglect the term here. The details of the dynamic procedure to obtain the estimate for $C_{\text{s}}\bar{\Delta}^2$ are provided in Section 3.3.

The sub-grid term

$$q_j^{\text{sgs}}=\bar{\rho}(\widetilde{Tu_j}-\tilde{T}\tilde{u_j}) \tag{36}$$

is described according to the derivation in [6] and is modeled using the eddy-viscosity hypothesis and a turbulent Prandtl number. The modeled expression is

$$q_j^{\text{sgs}}=\frac{\bar{\rho}C_{\text{s}}\bar{\Delta}^2|\tilde{S}|}{Pr_{\text{t}}}\frac{\partial\tilde{T}}{\partial x_j} \tag{37}$$

The turbulent Prandtl number Pr_{t} is evaluated using the dynamic procedure (see Section 3.3). *A priori* analysis of the magnitude of various terms in the filtered energy equation by Vreman *et al*. [24] has shown that the fourth and fifth terms on the right-hand side of Equation (34) are small compared with the sub-grid heat flux vector and can be neglected, especially at low and moderate Mach numbers. Finally, the last term in the filtered energy equation (Equation (34)) is similar to turbulent diffusion of sub-grid scale kinetic energy. The contribution of this term is

DOI: 10.1002/fld

again small compared with other sub-grid terms (see [6]), although there has been some attempts to model it (e.g. [31]). We neglected the term here.

3.3. Dynamic procedure

We employ a dynamic procedure to evaluate the constants in the modeled sub-grid terms. The dynamic model [26] is based on self-similarity of the inertial range of the turbulence energy spectrum at different length scales. Therefore, the same functional form for the sub-grid quantities can be assumed at the grid length scale $\bar{\triangle}$, representative of the computational mesh, and at a larger test filter length scale $\hat{\triangle}$. The residual stress at the test filter level, T_{ij}, appears when the test filter is applied to the grid filtered Navier–Stokes equation (Equation (33)). An identity due to Germano is then obtained by applying the test filter on the residual stresses at the grid filter level (τ_{ij}^{sgs}) and subtracting the resulting expression from T_{ij}:

$$L_{ij} = T_{ij} - \hat{\tau}_{ij}^{\mathrm{sgs}} = \widehat{\bar{\rho}\widetilde{u_i}\widetilde{u_j}} - \frac{\widehat{\bar{\rho}\widetilde{u_i}}\,\widehat{\bar{\rho}\widetilde{u_j}}}{\hat{\bar{\rho}}} \tag{38}$$

Assuming that the same functional form (Smagorinsky model) could be used for the residual stresses at both levels, we have the modeled forms as

$$T_{ij} = -2C_{\mathrm{s}}\hat{\triangle}^2\hat{\bar{\rho}}|\hat{\tilde{S}}|(\hat{\tilde{S}}_{ij} - \tfrac{1}{3}\hat{\tilde{S}}_{mm}\delta_{ij}) + \tfrac{1}{3}T_{kk}\delta_{ij} \tag{39}$$

$$\tau_{ij}^{\mathrm{sgs}} = -2C_{\mathrm{s}}\bar{\triangle}^2\bar{\rho}|\tilde{S}|(\tilde{S}_{ij} - \tfrac{1}{3}\tilde{S}_{mm}\delta_{ij}) + \tfrac{1}{3}\tau_{kk}^{\mathrm{sgs}}\delta_{ij} \tag{40}$$

Substituting the above two expressions into Equation (38), we obtain the modeled expression for L_{ij}:

$$L_{ij}^{\mathrm{mod}} = C_{\mathrm{s}}\bar{\triangle}^2 M_{ij} - \tfrac{1}{3}\tau_{kk}^{\mathrm{sgs}}\delta_{ij} + \tfrac{1}{3}T_{kk}\delta_{ij} \tag{41}$$

where M_{ij} is defined as

$$M_{ij} = 2\bar{\rho}|\tilde{S}|\widehat{\left(\tilde{S}_{ij} - \frac{1}{3}\tilde{S}_{mm}\delta_{ij}\right)} - 2\frac{\hat{\triangle}^2}{\bar{\triangle}^2}\hat{\bar{\rho}}|\hat{\tilde{S}}|\left(\hat{\tilde{S}}_{ij} - \frac{1}{3}\hat{\tilde{S}}_{mm}\delta_{ij}\right) \tag{42}$$

where typically $\hat{\triangle}/\bar{\triangle} = 2$ is assumed. Here, we neglect both τ_{kk}^{sgs} and T_{kk}. Finally, using Lily's [32] least-square minimization procedure we obtain

$$C_{\mathrm{s}}\bar{\triangle}^2 = \frac{L_{ij}M_{ij}}{M_{kl}M_{kl}} \tag{43}$$

where L_{ij} is explicitly given by Equation (38). This procedure gives a local time-dependent estimate of $C_{\mathrm{s}}\bar{\triangle}^2$, which is updated at each time iteration. It is worthwhile to note that the above procedure computes the Smagorinsky length scale $C_{\mathrm{s}}\bar{\triangle}^2$ directly without the need to specify the grid filter width $\bar{\triangle}$. This is advantageous in the current context considering that for unstructured hexahedral grid it is difficult to provide a general expression for the filter width $\bar{\triangle}$.

Since the solution, $\tilde{\mathbf{Q}}$, is discontinuous, the value of $C_{\mathrm{s}}\bar{\triangle}^2$ is also discontinuous across the sub-domains. The sub-grid length scale is used to evaluate the sub-grid momentum flux (Equation (35)), on which we impose continuity by averaging neighboring flux vectors. This is consistent with the flux continuity of the multidomain method.

DOI: 10.1002/fld

The turbulent Prandtl number (Equation (37)) is evaluated using a dynamic procedure similar to that described above. An expression similar to Germano's identity (Equation (38)) is obtained by subtracting the test filtered sub-grid heat flux ($\widehat{q_j^{\text{sgs}}}$) from the heat flux defined at the test filter level (Q_j):

$$K_j = Q_j - \widehat{q_j^{\text{sgs}}} = \widehat{\bar{\rho}\tilde{T}\tilde{u_j}} - \frac{\widehat{\bar{\rho}\tilde{T}}\,\widehat{\bar{\rho}\tilde{u_j}}}{\hat{\bar{\rho}}} \tag{44}$$

The same eddy diffusivity model is used for the heat flux at the test filter level:

$$Q_j = \frac{-C_s \hat{\bar{\rho}} \hat{\bar{\Delta}}^2 |\hat{\tilde{S}}|}{Pr_t} \frac{\partial \hat{\tilde{T}}}{\partial x_j} \tag{45}$$

Therefore, substituting Equations (37) and (45) into Equation (44), the modeled form for K_j is obtained as

$$K_j^{\text{mod}} = \frac{C_s \bar{\Delta}^2}{Pr_t} \left[\widehat{\bar{\rho}|\tilde{S}| \frac{\partial \tilde{T}}{\partial x_j}} - \hat{\bar{\rho}} \frac{\hat{\bar{\Delta}}^2}{\bar{\Delta}^2} |\hat{\tilde{S}}| \frac{\partial \hat{\tilde{T}}}{\partial x_j} \right] \tag{46}$$

Finally, following the procedure for computing the sub-grid viscosity, a least-square minimization technique is used for evaluating the sub-grid Prandtl number

$$Pr_t = \frac{2 N_i N_i}{K_j N_j} (C_s \bar{\Delta}^2) \tag{47}$$

where N_i is given by

$$N_i = \widehat{\bar{\rho}|\tilde{S}| \frac{\partial \tilde{T}}{\partial x_i}} - \hat{\bar{\rho}} 4 |\hat{\tilde{S}}| \frac{\partial \hat{\tilde{T}}}{\partial x_i} \tag{48}$$

assuming that $\hat{\bar{\Delta}}/\bar{\Delta} = 2$ and $C_s \bar{\Delta}^2$ is given by Equation (43).

3.4. Element level filtering

The dynamic procedure requires the definition of an explicit, low-pass filter for the test filtering operation. Spectral filtering can be constructed using either discrete polynomial transform (DPT) or interpolant projection (see [11]) over each element. DPT filtering can be conveniently applied for methods with modal basis. For methods with nodal basis, the solution has to be first transformed to modal basis before the DPT filter can be applied. Projection filtering, on the other hand, can be constructed directly on the nodal basis. Since it does not require an extra transformation, interpolant-projection filtering is more efficient than DPT for methods with nodal basis. Therefore, for our nodal basis we use an interpolant-projection filter.

In the interpolant-projection filtering procedure, the filtered variable of degree N is obtained by projecting the variable back and forth to a lower-order approximation of degree M defined on

DOI: 10.1002/fld

a subset of the original nodal values. As a first step the original function is interpolated from a polynomial degree, N, to a polynomial of lower degree, M:

$$Q'(x_i) = \sum_{j=0}^{N} L_j(x_i) Q(\bar{x}_j) \tag{49}$$

where x_i, $\bar{x}_j$ are the nodes corresponding to $\mathbf{P}_M$ and $\mathbf{P}_N$, respectively. $L_j \in \mathbf{P}_N$ is the Lagrange interpolating polynomial. The above operation can be cast in terms of matrix–vector product:

$$Q'_i = I^{\text{int}}_{ij} Q_j \tag{50}$$

where

$$I^{\text{int}}_{ij} = \prod_{k=0, k\neq j}^{N} \frac{x_i - \bar{x}_k}{\bar{x}_j - \bar{x}_k}, \quad i = 0, \ldots, M, \quad j = 0, \ldots, N \tag{51}$$

In the second step the function $Q'(x)$ is projected back to the polynomial space N giving the filtered function

$$Q^{\text{filt}}(\bar{x}_e) = \sum_{f=0}^{M} L_f(\bar{x}_e) Q'(x_f) \tag{52}$$

Again, the above can be cast in matrix–vector form

$$Q^{\text{filt}}_e = I^{\text{pro}}_{\text{ef}} Q'_f \tag{53}$$

with

$$I^{\text{pro}}_{\text{ef}} = \prod_{k=0, k\neq f}^{M} \frac{\bar{x}_e - x_k}{x_f - x_k}, \quad e = 0, \ldots, N, \quad f = 0, \ldots, M \tag{54}$$

In the staggered-grid method, this interpolation–projection operation could be applied to both the nodal sets (Gauss–Gauss and Gauss–Lobatto nodes). We apply the filter on the Gauss–Lobatto basis since it preserves the end values of the original function and ensures C_0 continuity.

4. TESTING THE LES METHOD

We test the performance of the staggered-grid, multidomain LES method for two different classes of turbulent flows. The first case study is on an isotropic decaying turbulence, and enables a first-order investigation of the characteristics of the LES method, since the flow does not involve turbulence shear production and specification of boundary conditions. Many sub-grid models have been calibrated with this flow (e.g. [26, 33]). Then, we perform a more complex test by simulating a plane, parallel channel flow at two different Reynolds numbers, which does involve boundary condition specification and shear production.

4.1. Decaying isotropic turbulence

Computation of the decaying isotropic turbulence is performed within a periodic box of size 2π. An initial correlated turbulence flow field is specified according to the procedure outlined by Rogallo

DOI: 10.1002/fld

Table I. Cases for decaying isotropic turbulence simulation.

Case	$h_x \times h_y \times h_z$	p	M
DNS-RES	$6\times6\times6$	15	NA
DNS-URES	$6\times6\times6$	8	NA
LES-BASE	$6\times6\times6$	8	$(N+1)/2$
LES-RFNDp	$6\times6\times6$	10	$(N+1)/2$
LES-FILT	$6\times6\times6$	8	$N-2$
LES-RFNDh	$7\times7\times7$	8	$(N+1)/2$

[34] using a specified energy spectrum. We take an initial energy spectrum that was modeled in Blaisdell *et al*. [35]. We refer to this spectrum and case as BMR93. The spectra are purely solenoidal (divergence free) and there is no fluctuation in the thermodynamic variables. The spectra are top hat and have non-zero contributions in the wavenumber range of $8\leqslant k\leqslant16$. The initial flow field for velocities (u, v, w), density (ρ), and temperature (T) is obtained on a uniform grid from the Fourier coefficients using a fast Fourier transform. The resultant flow field is correlated according to the top hat spectra. Finally, the initial flow field on the Chebyshev–Gauss points is obtained by interpolating from the Fourier grid using an eighth-order Lagrangian interpolation. The interpolation was shown to be adequately accurate even for low polynomial orders in [16]. The initial root mean square (rms) Mach number is 0.3 with a peak $Re_\lambda\approx40$.

4.1.1. Resolution and spectra. We start by establishing resolution requirements for a resolved LES and the effect of resolution on the accurate representation of the spectrum. To this end, we computed several cases with different h and p resolutions that are summarized in Table I. The number of sub-domains in x, y, and z directions is given by h_x, h_y, and h_z, while p represents the order of polynomial in each sub-domain. LES-BASE is the base case with six domains in each directions and $p=8$. LES-RFNDp and LES-RFNDh have a finer resolution of $p=10$ and $h=7$, respectively. The DNS-RES and DNS-URES, respectively, refer to resolved and unresolved DNS without filtering.

The total energy spectra in Figure 2 show that the resolved DNS (DNS-RES) is in good agreement with previously published BMR93 data. The sharp, matching drop-off in the spectra indicates that the DNS is resolved. The BMR93 case was computed with a Fourier-spectral method with 96^3 grid points. DNS-RES uses a comparable amount of degrees of freedom with $h=6$ domains in each direction and $p=15$, yielding $h*(p+2)=102$ Lobatto points in each direction, to resolve the flow. This is consistent with the validation study in [16].

Comparison of the energy and dissipation spectra between DNS-URES, LES-BASE, and the resolved DNS-RES (Figure 2) reveals that LES is clearly capturing the drop-off in the spectra better than the under-resolved DNS. A zoom-in on the high-frequency part ($k\geqslant7$) of the spectrum in Figure 3 underscores the improved capturing. LES-BASE resolves the flow up to $k\approx20$, while the increase of the spectrum for $k\geqslant12$ of the coarse DNS indicates an inaccurate solution. The dashed-dashed line in the figure highlights the point up to which there is agreement between the BMR93 spectra and DNS-URES, while the dashed-dot line shows the same for LES-BASE. Clearly, the sub-grid model in LES is correctly modeling the dissipative effect of the small scale on the turbulence, which leads to the steep drop-off of the spectrum at high wavenumbers. While in a resolved DNS these small scales are accurately captured, in the under-resolved DNS insufficient

DOI: 10.1002/fld

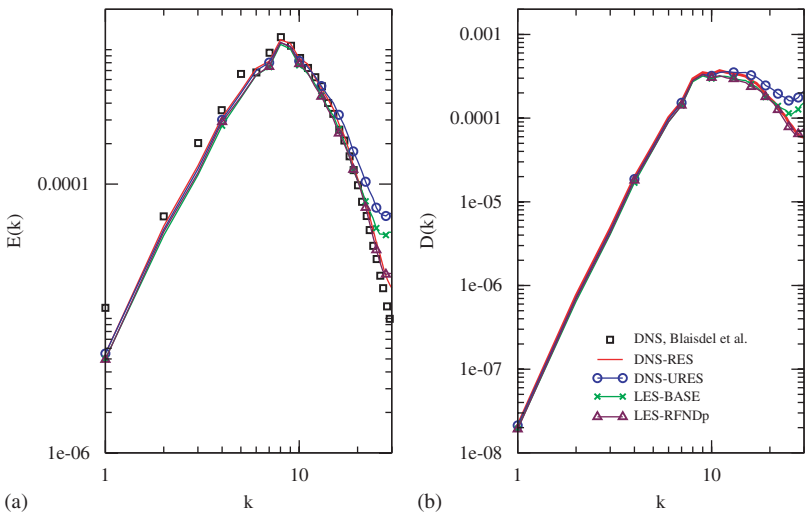

Figure 2. Comparison of (a) energy spectra and (b) dissipation spectra at $t = 3.2$ for isotropic turbulence.

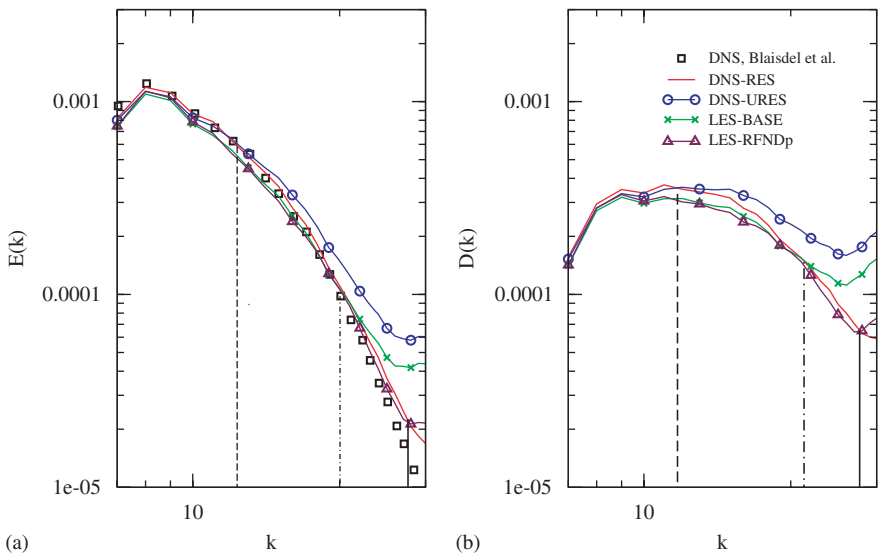

Figure 3. Same as Figure 2, zoomed in on high wavenumbers.

resolution is unable to accurately compute the high-frequency spectrum. Instead, the numerical errors determine the behavior at the small scale. In a numerical method with very small dissipation such as the multidomain spectral method, the numerical errors are not dissipated as in dissipative method (e.g. upwind schemes). Rather, the numerical errors pile up at high wavenumbers, as seen in the spectra. In LES, the scales up to $k = 20$ are numerically resolved. At $k \geqslant 12$ the LES sub-grid model accurately models the dissipative term to the filtered equations.

DOI: 10.1002/fld

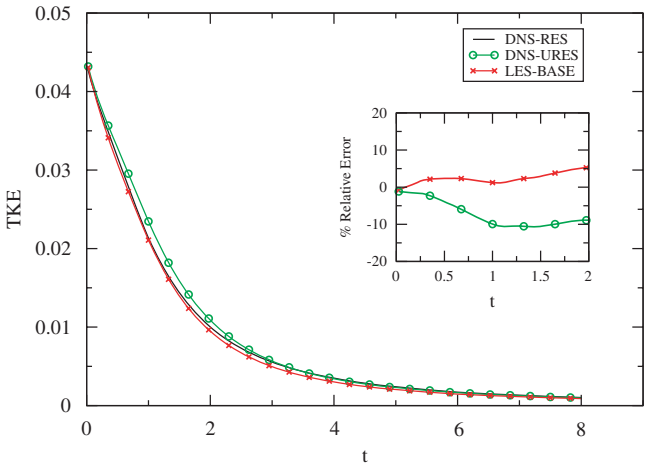

Figure 4. Decay of turbulent kinetic energy for isotropic turbulence. Inset: the relative error for cases LES-BASE and DNS-URES.

Comparison of the turbulence kinetic energy (tke) decay rate for DNS-RES, DNS-URES, and LES-BASE in Figure 4 confirms the improved dissipation modeling. At $t=2$, 75% of the initial energy has decayed. The decay rate determined with LES is in closer agreement with DNS-RES than the rate determined with DNS-URES. DNS-URES under-predicts the decay rate. The additional dissipation provided by the sub-grid model in LES increases the turbulence dissipation and improves comparison with DNS-RES. In the inset of Figure 4 we plot the percentage relative error, defined as $(\text{tke}_{\text{DNS-RES}} - \text{tke})/\text{tke}_{\text{DNS-RES}} \times 100$, for LES-BASE and DNS-URES. On average, the magnitude of the error for the coarse DNS is twice that of the LES case.

We assess the resolution requirement for LES with multidomain Chebyshev method from the cut-off wavenumber ($k_c = 20$). The total number of Lobatto points in each direction is 60 (6 sub-domains $\times$ 10 Lobatto points). This implies that in order to resolve the spectrum till $k=20$, 3 points are needed per wavelength. The value is further confirmed by the refined LES case (LES-RFNDp), where the total number of Lobatto points is 72 (6 sub-domains $\times$ 12 Lobatto points) and the flow is resolved up to $k=27$ (the cut-off is marked by the solid line). Therefore, again $72/27 \approx 3$ points are required per wavelength. This resolution is consistent with the requirements reported in [16].

4.1.2. Dilatational and thermodynamic field. Decomposition of the velocity spectrum into solenoidal (Figure 5(a)) and dilatational spectra (Figure 5(b)) shows that the dilatational spectrum is two orders of magnitude less than the solenoidal spectrum, which is in agreement with BMR93. The solenoidal velocity is associated with vorticity [36]. The vortical mode can generate both larger length scales, through vortex merging, and smaller scales, through vortex stretching. Therefore, the initial top hat solenoidal spectrum smoothes out at both low and high wavenumbers in time.

The dilatational velocity is associated with the acoustic and entropy mode [36]. In the acoustic mode small length scales are generated through non-linear steepening of pressure waves, but there is no direct mechanism for generation of larger length scales as in the solenoidal mode. Since the simulation is started with zero fluctuations in dilatational velocity and thermodynamic fields, the acoustic fluctuations were created through non-linear production from the solenoidal velocity

DOI: 10.1002/fld

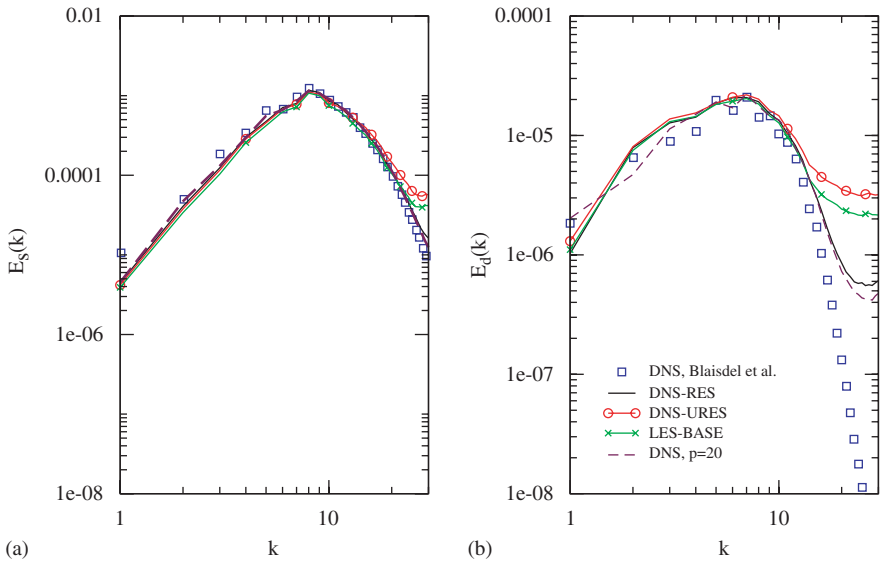

Figure 5. Comparison of decomposed energy spectra at $t = 3.2$ for isotropic turbulence: (a) solenoidal spectrum and (b) dilatational spectrum.

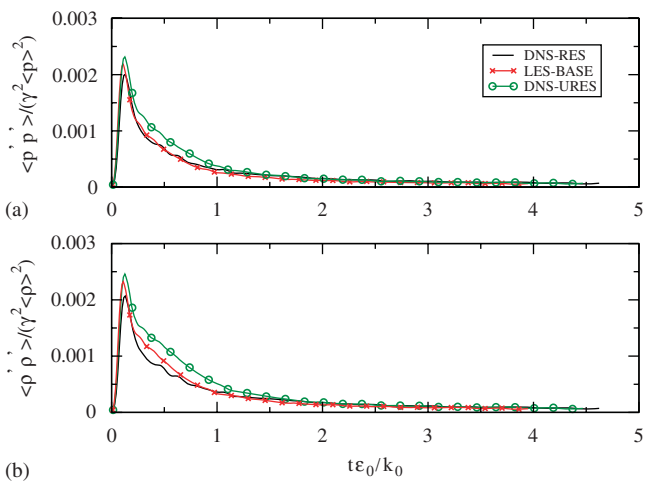

Figure 6. Decay of (a) pressure and (b) density fluctuations.

field. For small turbulent Mach numbers, the length scale of the acoustic fluctuations generated from the vorticity fluctuations is much larger than the length scale of vortical turbulence [16, 35]. In time the acoustic length scales grow to become comparable to the size of the simulation box and hence cannot be resolved. As a result the dilatational velocity spectra have a very flat character at low wavenumbers. Case DNS-RES shows good agreement for the dilatational spectrum

DOI: 10.1002/fld

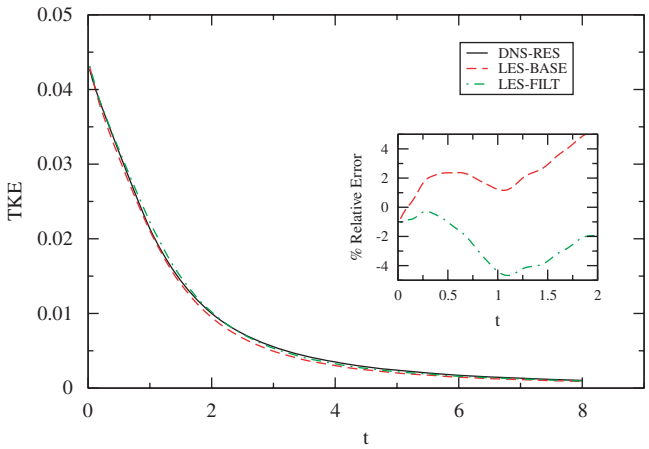

Figure 7. Decay of turbulent kinetic energy for DNS and LES with different test filter strengths. Inset: the relative error for cases LES-BASE and LES-FILT.

up to $k=15$, but the sharp drop-off at high wavenumbers as in BMR93 is not observed. Since the dilatational spectrum is two orders of magnitude less than the solenoidal spectrum, a much higher resolution is required to capture the drop-off. This is evident from Figure 5(b), where the spectrum for a DNS case with $p=20$ and $h=6$ shows better agreement with BMR93. However, the dilatational spectrum has a very small contribution to the total spectrum and therefore the case DNS-RES, which accurately resolves the solenoidal spectrum, is considered as the resolved DNS. The dilatational spectra for the case LES-BASE are closer to BMR93 than DNS-URES (coarse DNS). The normalized fluctuations of pressure and density are shown in Figure 6 for cases DNS-RES, DNS-URES, and LES-BASE. Both pressure and density fluctuations initially grow with time as energy is drained from the velocity field. After attaining peaks, which are approximately same for both the quantities, they start decaying. The figure shows that LES-BASE predicts a more accurate decay than DNS-URES.

4.1.3. Test filter effect. The Lagrange-interpolant-projection filtering requires two sets of Lobatto grids (Section 3.4). The polynomial space of degree N is fixed by the polynomial approximation used within each sub-domain for the flow computation, i.e. $N=10$ when $p=N-2=8$. On the other hand, the size of the lower-degree grid of order M used for the interpolation can be varied independently and determines the strength of the test filter. With decreasing M, the strength and consequently the effect of the filter is larger. To investigate how the degree M of the lower-order grid affects the flow, LES results based on two test filters are compared and listed as LES-BASE and LES-FILT in Table I. The lower-order grid for the test filter of LES-BASE is of degree $M=(N+1)/2$, while the test filter in LES-FILT is of degree $M=N-2$.

The decay of tke for the two LES cases is compared with DNS-RES in Figure 7. The percentage relative errors are shown in the inset of the figure. LES-BASE has a lower error for $t<1$, while for $t>1$ the error magnitude is lower for LES-FILT. For both cases the predictions are within 5% of the reference case, indicating that the choice of the filter strength has small influence on the decay of tke, since the sub-grid viscosities are nearly equal in both cases. Decays of normalized

DOI: 10.1002/fld

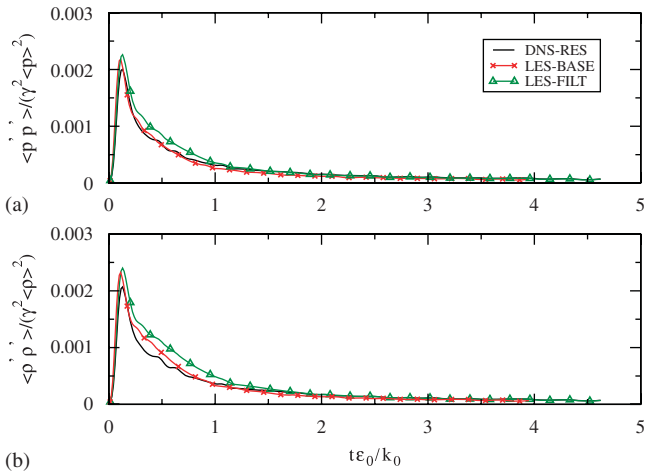

Figure 8. Decay of (a) pressure and (b) density fluctuations for DNS and LES with different test filter strengths.

fluctuations of pressure and density (shown in Figure 8), however, show considerable differences. For both quantities, the decay rate for LES-FILT has larger deviation from the reference DNS case (DNS-RES) as compared with LES-BASE. Energy cascade in the acoustic and entropy mode is linked to much faster time scale of evolution than the solenoidal mode. Therefore, the LES cases, which are inherently under-resolved, fail to capture some of these fine-scale acoustic phenomenon. The weaker test filter ($M = N - 2$) possibly allows faster accumulation of numerical noise, thereby contaminating the solution at the highest resolved wavenumber. This causes the error in the decay of the thermodynamic quantities. With a stronger test filter, on the other hand, the numerical noise is eliminated and the acoustic scales are better represented. Therefore, we conclude that when the effect of the test filter is larger, more small-scale acoustic waves are modeled.

4.1.4. h/p Resolution study. One of the distinguishing aspects of spectral/hp element methods is the feature of controlling the spatial resolution at two different levels. The resolution can be altered either by changing the number of sub-domains (h-refinement) or by changing the order of the polynomial within each sub-domain (p-refinement).

Here, we study the effect of independently changing the h and p resolutions on the LES results. Cases LES-BASE and LES-RFNDp have the same h-grid but different polynomial orders, while cases LES-BASE and LES-RFNDh have the same polynomial order but different h-grids. The total number of Lobatto points for cases LES-RFNDp and LES-RFNDh is 72 and 70, respectively, which is comparable. The total energy spectra for cases LES-BASE, LES-RFNDp, and LES-RFNDh are shown in Figure 9. As the polynomial order is increased from $p = 8$ (LES-BASE) to $p = 10$ (LES-RFNDp), the maximum resolved wavenumber increases from $k = 20$ (the cut-off is marked by the dashed-dashed line) to $k = 27$ (the cut-off is marked by the solid line). Whereas, increasing the number of sub-domains in each direction from $h = 6$ (LES-BASE) to $h = 7$ (LES-RFNDh), the maximum resolved wavenumber increases to $k = 25$ (the cut-off is marked by the dashed-dot line). This indicates that p-refinement resolves the flow better than h-refinement, which is consistent with the h/p spectral convergence [9].

DOI: 10.1002/fld

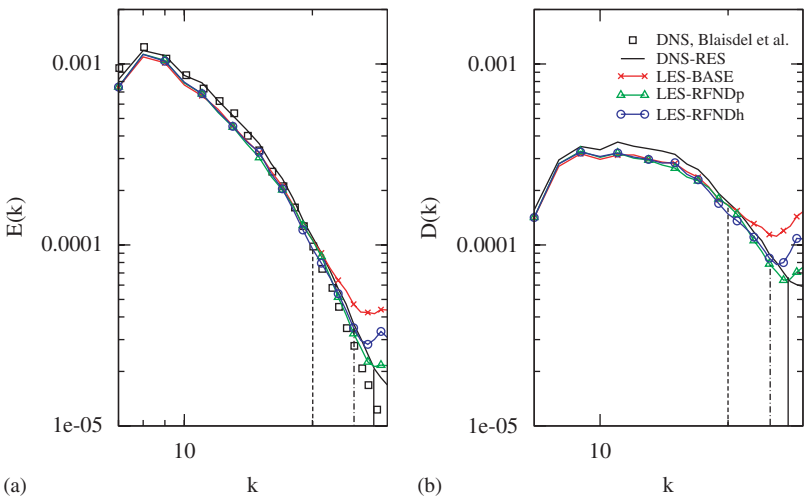

Figure 9. h/p Resolution study: (a) energy spectra and (b) dissipation spectra.

4.1.5. Explicit filtering without the sub-grid model. Recently an alternate approach to LES, which does not involve any sub-grid modeling, has been proposed (see [37–39]). Domaradzki *et al.* [37] applied a periodic filtering to the flow variables in their under-resolved spectral simulations without employing any sub-grid model. Bogey and Bailly [39] applied a similar technique for their high-order finite difference simulation of compressible jets. A selective filter was applied to the density, momentum ρu_i, and pressure to remove the high wavenumbers close to the grid cut-off. The filter was designed to eliminate grid-to-grid oscillations without affecting the resolved scales.

The above studies motivated us to investigate the effect of using simply a Lagrange-interpolant filter (described in Section 3.4) for an under-resolved simulation, without including the sub-grid model. The filter is applied at every time step on density, momentum ρu_i, and pressure for a case having the same resolution as DNS-URES. It is imperative to use a filter that does not affect the large scales of the flow but at the same time prevents the numerical noise (inherent in under-resolved simulations with high-order methods) from contaminating the solution at high wavenumbers. Therefore, we test filters of different strengths to determine the most effective filter. Figure 10 compares the spectra for three different filters with the resolved DNS. We observe that the filter ($M=N-3$) affects the large scales resulting in an inaccurate representation of the spectra at low wavenumbers. For filters stronger than $M=N-3$ the solution was not stable. On the other hand, the use of weaker filters ($M=N-1$ and $M=N-2$) resolves the large scales accurately, with $M=N-2$ providing a slightly better drop-off of the spectra.

We further investigate the role of the filter by comparing the spectra with that of the LES with the sub-grid model (LES-BASE). Figure 11 shows the spectra from the filtering case $M=N-2$ (DNS-URES-FILT) along with DNS-URES and LES-BASE. Comparison of DNS-URES and DNS-URES-FILT reveals that filtering of the solution slightly improves the spectra. While DNS-URES captures the spectra up to $k=12$, DNS-URES-FILT is accurate up to $k=14$. However, LES-BASE is more accurate than DNS-URES-FILT, implying that for our multidomain spectral simulations, the use of only a filter does not provide adequate dissipation and the SGS model is necessary to account for the sub-grid dissipation accurately.

DOI: 10.1002/fld

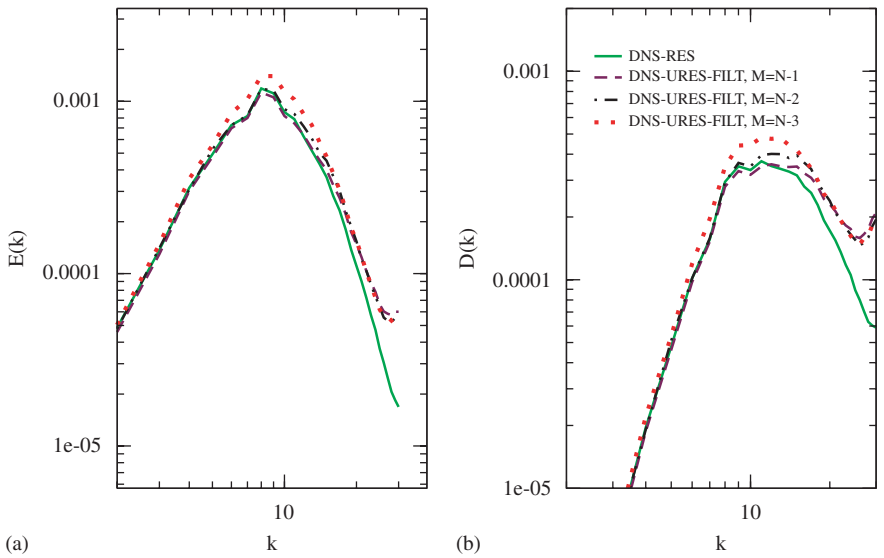

Figure 10. Effect of filtering the under-resolved simulation (no SGS model) with different filter strengths: (a) energy spectra and (b) dissipation spectra.

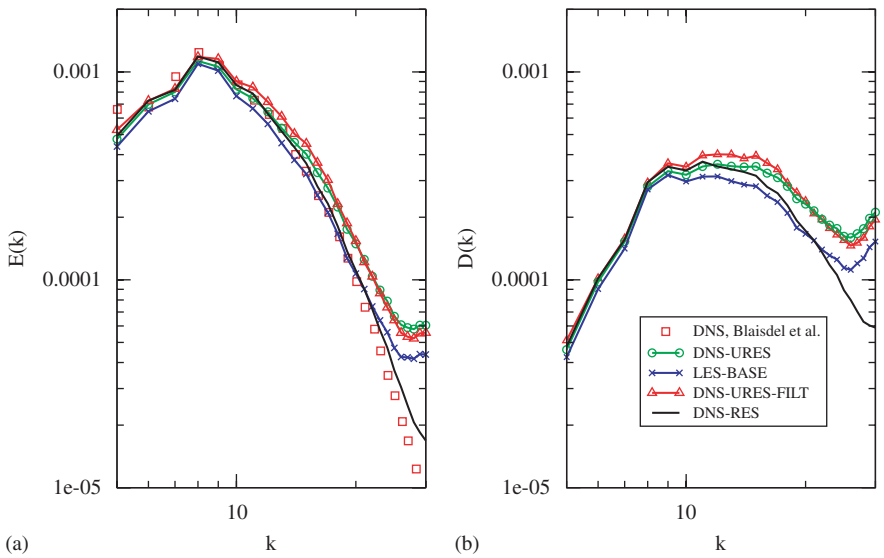

Figure 11. Comparison of explicit filtering and SGS model as the sub-grid dissipative mechanism: (a) energy spectra and (b) dissipation spectra.

4.2. Turbulent channel flow

Next, the LES methodology is tested for a three-dimensional, subsonic, plane, parallel channel flow. The presence of the wall significantly increases the complexity of the flow, the analysis,

DOI: 10.1002/fld

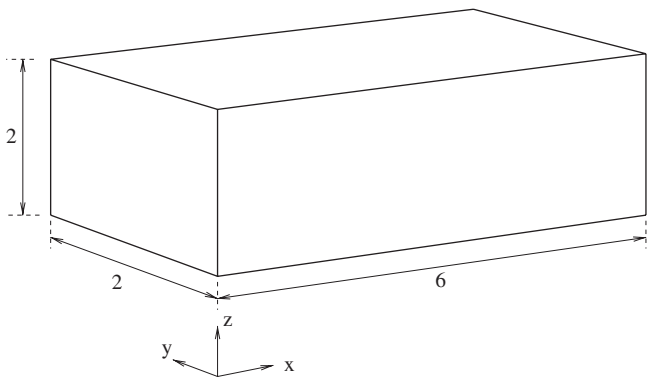

Figure 12. Schematic of channel flow geometry (not to scale).

and the LES implementation as compared with the isotropic turbulence case. Traditionally, the near wall region in LES of wall-bounded flows is either resolved with a fine mesh like in DNS or modeled [40]. Moin and Kim [41] performed LES of incompressible channel flow, with a Fourier-spectral-finite difference scheme using a non-dynamic eddy-viscosity model. Application of the dynamic Smagorinsky model to incompressible channel flow at high Reynolds numbers was studied by Piomelli [42], where a Fourier–Chebyshev pseudo-spectral collocation scheme was used. Wang and Pletcher [43] performed LES of low-speed flows with significant heat transfer at the wall, using a low-Mach-number algorithm coupled to a dynamic eddy-viscosity model. LES of compressible channel flow in both subsonic and supersonic regimes, at a bulk Reynolds number of 3000, was performed by Lenormand *et al*. [44]. They used fourth- and second-order finite difference to discretize the convective and diffusive terms, respectively. The sub-grid scales were represented through Smagorinsky and scale similarity models. Channel flow was also used for validating LES methodologies with finite element (e.g. [5]) and spectral element (e.g. [11]) methods. In [5] it was shown that the finite element method gave better prediction of the normal Reynolds stresses over a second-order central difference scheme. In their validation study, Blackburn and Schmidt [11] found that test filtering in Legendre basis gave the best result for the mean velocity profile, while the projection filter provided the best agreement with DNS for both normal and shear stresses.

4.2.1. Computational model. A schematic of the computational domain is shown in Figure 12. The domain extents are $L_x=6$, $L_y=2$, and $L_z=2$ in the streamwise, spanwise, and wall-normal directions, respectively. Periodic boundary conditions are employed in the streamwise and spanwise directions, while the conservative isothermal wall boundary condition of Jacobs *et al*. [45] is used for the bottom and top walls. The flow is simulated at bulk Reynolds numbers of $Re_f=3000$ and 10000 based on channel half width and bulk velocity. The corresponding friction Reynolds numbers were $Re_\tau\approx 180$ and $Re_\tau\approx 570$, respectively. The Mach number is taken to be $Ma=0.4$ based on bulk velocity and wall temperature (T_{wall}). Following Lenormand *et al*. [44], a time-dependent forcing term is included in the streamwise momentum equation in order to drive the flow. The velocity field is initialized with the laminar parabolic profile for u with a small random

DOI: 10.1002/fld

disturbance superimposed on it:

$$u(z) = -6\left[\left(\frac{z}{2}\right)^2 - \frac{z}{2}\right](1+\varepsilon), \quad v=0, \quad w=0 \tag{55}$$

where ε is a 10% random disturbance. The temperature is initially set to laminar Poiseuille profile:

$$T(z) = T_{\text{wall}} + \left\{\frac{3(\gamma-1)}{4Pr}[1-(z-1)^4]\right\} \tag{56}$$

Here $T_{\text{wall}}=6.25$ is the wall temperature and $Pr=0.72$ is the Prandtl number. The density is initially set as constant. The initial pressure is calculated from the constant density, the initial temperature, and the ideal gas law. Previous studies [16, 46] have shown that at $Ma=0.4$, plane parallel channel flow is pseudo-incompressible. Therefore, our simulation results are compared with the incompressible DNS study of Moser *et al*. [47] and the experimental measurements of Niederschulte *et al*. [48].

4.2.2. Low-Reynolds-number simulation. The first test case is for $Re=3000$. This is close to the lowest Reynolds number at which a fully developed turbulent channel flow can be sustained without relaminarization. The computational domain (Figure 12) is decomposed with 10 sub-domains in the streamwise (x) and spanwise (y) directions, while 16 sub-domains are taken in the wall-normal (z) direction. The sub-domains in the wall direction are stretched out toward the center of the channel with a cosine distribution. The polynomial order within each sub-domain is taken as $p=6$. The total number of Lobatto points for the above h/p grid is 819 200. The test filtering is performed along all the coordinate directions. It is known that when the filter is a function of space, as is the case for a non-uniform grid, additional terms appear in the filtered Navier–Stokes equation (see [49]). However, the magnitude of these terms is small when the grid non-uniformity is not large. An LES simulation of isotropic turbulence with a non-uniform sub-domain distribution confirmed this. The spectra of the non-uniform sub-domain computation (not shown) were in excellent agreement with the uniform grid simulation. Therefore, the use of non-uniform sub-domains for the channel flow does not pose a problem. The sub-grid constant $C_s\bar{\Delta}^2$ and Pr_t are obtained by averaging the right-hand side of Equations (43) and (47) along homogeneous (x–y) planes within each sub-domain:

$$C_s\bar{\Delta}^2 = \left\langle \frac{L_{ij}M_{ij}}{M_{kl}M_{kl}} \right\rangle, \quad Pr_t = \left\langle \frac{2N_iN_i}{K_jN_j} \right\rangle (C_s\bar{\Delta}^2) \tag{57}$$

where $\langle\rangle$ indicates averaging. This averaging technique was proposed by Zhao and Voke [50] and was shown to be more stable and give better agreement with the asymptotic behavior of turbulent length scales near the wall as compared with the Germano–Lily averaging approach [26]. The sub-grid viscosity is computed once in every time step.

The Favre-averaged streamwise velocity normalized with the skin friction velocity, plotted in Figure 13, is in close agreement with that in Moser *et al*. [47] near the wall. The maximum relative error of the LES prediction in the near wall region is 7%. Therefore, the dynamic model is able to represent the near wall structures accurately. This observation is consistent with previous implementations of the dynamic Smagorinsky model with both finite difference and finite volume methods. The LES result is also compared with the 'law of the wall' in the figure. The LES result matches with the linear $u^+=z^+$ law in the viscous sub-layer ($z^+\leqslant 5$). The agreement in the log-layer

DOI: 10.1002/fld

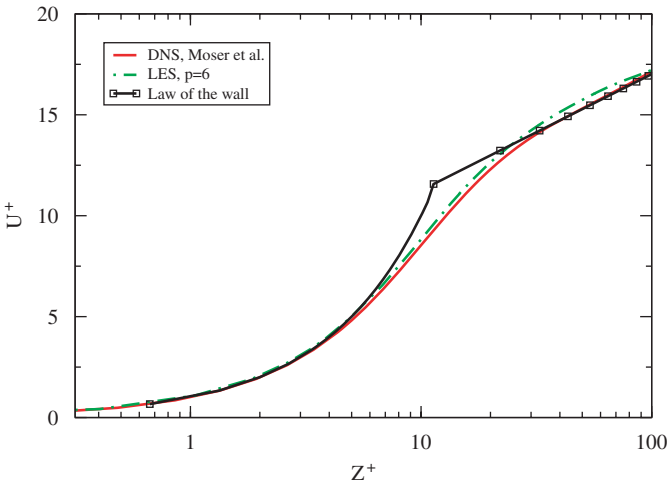

Figure 13. Mean normalized streamwise velocity plotted in wall coordinates for channel flow at $Re = 3000$.

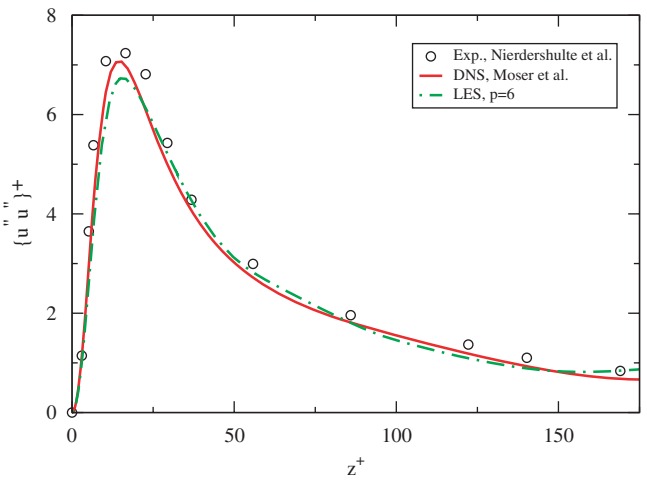

Figure 14. Streamwise normal stresses for channel flow at $Re = 3000$.

is also good, the maximum deviation from the reference data being only 3%. It can be concluded that the first-order statistics are accurately recovered by LES, with approximately one-third the resolution of DNS by Jacobs *et al*. [16], who used the same Chebyshev spectral multidomain method, and Moser *et al*. [47], who used a pseudo-spectral code. The gain in computational time is slightly offset by the computational overhead of the sub-grid model. The cost of LES was 1.44 times that of the simulation without the sub-grid model on the same grid.

In Figure 14, the resolved-scale Favre-fluctuating streamwise turbulent stress computed with LES is compared with the DNS and the experiment. The results are normalized with u_τ^2 and plotted in wall coordinates. It is noted that although the usual practice in *a posteriori* testing is to compare

DOI: 10.1002/fld

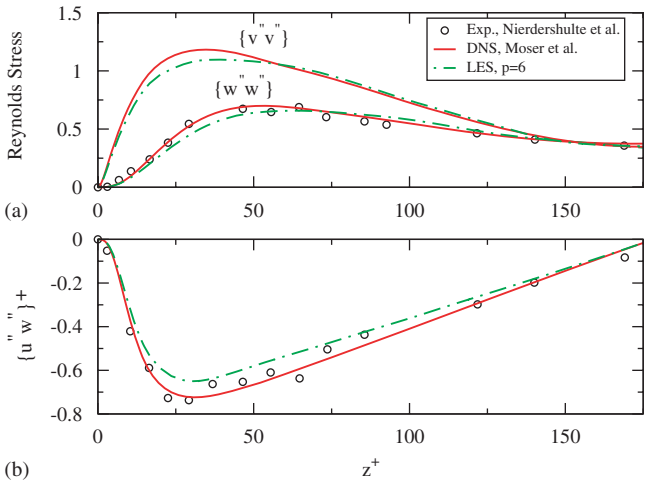

Figure 15. (a) Normal stresses in the spanwise and wall-normal directions and (b) shear stress for channel flow at $Re = 3000$.

the resolved-scale Reynolds stresses from LES directly with unfiltered DNS or experiment, the two quantities are not equivalent and therefore are not expected to match exactly. The location for the peak streamwise fluctuation is accurately represented by LES, although there is a 4% under-prediction in the magnitude of the peak. Except for the peak value, the resolved-scale stress from LES compares well with the DNS and the experiment. The Favre-fluctuating spanwise ($\{v''v''\}^+$) and wall-normal ($\{w''w''\}^+$) stresses are shown in Figure 15(a). The peak $\{v''v''\}^+$ and $\{w''w''\}^+$ values are under-predicted by 6% and 9%, respectively. The otherwise overall good agreement in the normal stresses indicates that the primary energy containing motions are resolved in the simulation. Finally, Figure 15(b) shows that LES under-predicts the resolved-scale shear stress, with a maximum difference of 10% with the DNS. The experimental data show a large scatter across the channel.

4.2.3. High-Reynolds-number simulation. LES is considered robust if it is stable and accurate at a high Reynolds number with a coarse grid. Here, we demonstrate the robustness of our LES methodology by simulating the same channel configuration as in the previous section at a Reynolds number of $Re_f = 10000$ ($Re_\tau \approx 570$). We keep the h resolution the same as before, while increasing the polynomial order within each sub-domain to $p = 8$. The total number of Lobatto points is 1.6 million. The LES results are compared with DNS data of Moser *et al.* [47] for $Re_\tau \approx 590$.

Figure 16 shows that the LES mean velocity profile in wall coordinates is in close agreement for $z^+ < 10$ with DNS as in the low-Reynolds-number channel flow. The linear law of the wall is well represented by LES. However, there are differences for $z^+ > 10$, where the LES under-predicts the mean velocity. The under-prediction is attributed to the under-resolution in the outer layer and the type of test filter used here. The number of grid points used for DNS is a factor of 20 times larger than the number of grid points used for LES. The effect of under-resolution was investigated in several studies. In Bagget *et al.* [51] the resolution requirement for LES of shear flows using the dynamic Smagorinsky model was studied through a series of channel flow simulations at a

DOI: 10.1002/fld

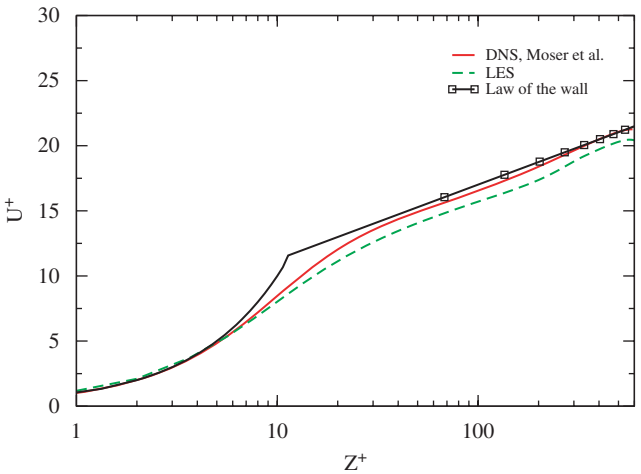

Figure 16. Mean normalized streamwise velocity plotted in wall coordinates for channel flow at $Re=10000$.

high Reynolds number ($Re_\tau \approx 1000$). They varied the resolution in the outer layer while keeping the near wall mesh the same, which essentially resolved the near wall structures. It was shown that the sub-grid shear stress predicted by the dynamic model in *a posteriori* simulation was less than the shear stress obtained using filtered DNS data. Such under-prediction in shear stress directly affects the averaged velocity profile. Using the data from [51], Jimenéz and Moser [52] showed that the fractional error in prediction of mean velocity is roughly proportional to and is of the same order as the fraction of shear stress carried by the sub-grid model. Therefore, they concluded that the prediction in mean velocity can be improved by adjusting the resolution so that the amount of shear stress carried by the sub-grid model is small. Under-prediction in the averaged velocity was also observed by Blackburn and Schmidt [11], for their spectral element LES using interpolant-projection-type filtering.

Figure 17 compares the resolved-scale Favre-fluctuating streamwise turbulent stress, again normalized with u_τ^2, from LES with Moser *et al*. The location of the peak is again accurately captured by LES, while the magnitude is under-predicted by 4%. In contrast to the low-Reynolds-number case, where an excellent agreement was seen, the LES stresses have slightly lower value for $z^+ > 70$, with a maximum under-prediction of 13% at $z^+ = 200$. The spanwise ($\{v''v''\}^+$) and wall-normal ($\{w''w''\}^+$) turbulent stresses, shown in Figure 18(a), on the other hand, show a slight over-prediction for $z^+ < 300$, the maximum differences being 11% and 7%, respectively. The over-predicted stresses are attributed to the under-resolution and the modeling of the sub-grid stresses. In *a posteriori* LES it is generally difficult to isolate the effect of grid resolution and the sub-grid model on the Reynolds stresses, especially for inhomogeneous flows.

However, it was shown in [53] that the flow tends to be over-dissipative at a marginal resolution resulting in an over-prediction of normal stresses. Such an over-prediction of stresses across the channel was also observed in the spectral element simulation of Blackburn and Schmidt [11]. The resolved-scale shear stress (Figure 18(b)) is also in good agreement with the DNS data. The values are over-predicted till $z^+ < 300$, with a maximum difference of 3.5%.

DOI: 10.1002/fld

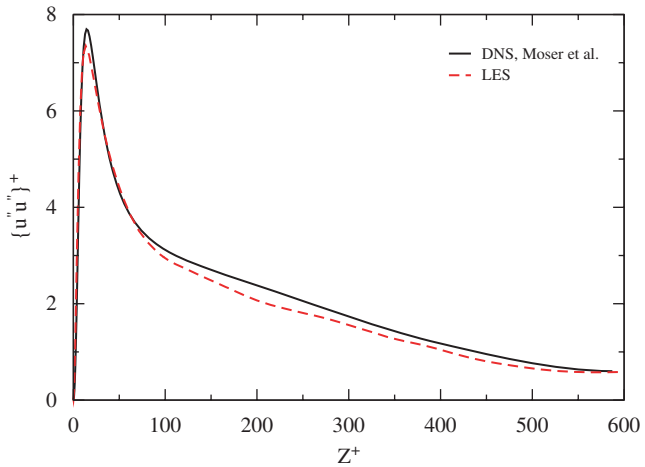

Figure 17. Streamwise normal stresses for channel flow at $Re = 10000$.

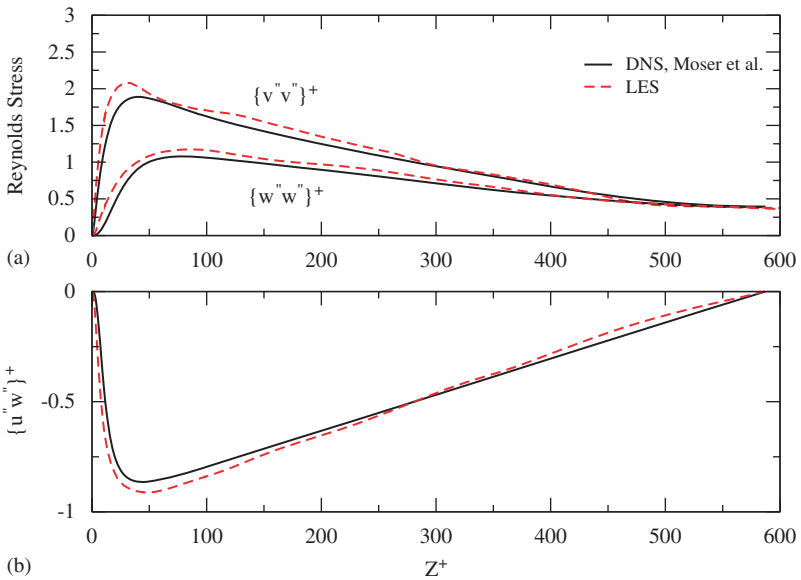

Figure 18. (a) Normal stresses in the spanwise and wall-normal directions and (b) shear stress for channel flow at $Re = 10000$.

5. CONCLUSIONS

A robust, high-order, spectral element large-eddy simulation (LES) technique for compressible flow has been developed. The high-order Chebyshev approximation controls the numerical errors,

DOI: 10.1002/fld

while the flux-based method ensures a conservative scheme. The sub-grid stress and sub-grid heat flux are represented by dynamic models, which, in combination with the unstructured multidomain method, facilitate a flexible methodology that could be applied for complex flow geometries.

The evaluation of the LES code in a decaying isotropic case at $Re_\lambda \approx 40$ and $Ma_{\text{rms}} = 0.3$ reveals that the LES method computes the turbulence spectrum far more accurately than does the under-resolved DNS. Since the numerical method has very little dissipation, the numerical error generated in the under-resolved DNS computations increases the energy in the high-frequency part of the energy spectrum. The LES model correctly models the physical dissipation and agrees with the spectrum of a resolved DNS. The current LES method improves over lower-order LES methods that can have numerical dissipation, thus lowering the energy in the high-frequency range. The rate of decay of tke and fluctuations in thermodynamic quantities are more accurate for LES than for coarse DNS. Lack of numerical dissipation in a higher-order LES method enables a reliable analysis of the role of the sub-grid model and test filtering in *a posteriori* computation. From the cut-off wavenumbers for the LES cases, we deduce that the multidomain LES requires only 3 Lobatto grid points per resolved-scale wavenumber, which is significantly less than the lower-order LES requirements. The study of the effect of the test filter strength indicates that $M = (N+1)/2$ results in better prediction of the decay of thermodynamic fluctuations than $M = N-2$, where N is the degree of the Lobatto grid used for the solution, while M is the degree of the lower-order Lobatto grid used for constructing the test filter. Analysis of p and h convergence for LES demonstrates that p-refinement is more efficient than h-refinement, which is consistent with the h/p convergence theory. Investigation into the effect of filtering the under-resolved DNS without employing the sub-grid model reveals that though the spectrum improves with filtering, it is still much less accurate than the case with the sub-grid model. This implies that using only a filter does not provide adequate dissipation to drive the energy cascade to the unresolved scales and the use of the sub-grid model becomes imperative.

LES tests on the turbulent channel flow with the near wall area resolved illustrate the success of the new LES methodology to predict wall-bounded, inhomogeneous turbulent flows at low and moderately high Reynolds numbers. LES of the channel flow at $Re = 3000$ shows that the method accurately computes the flow for $z^+ < 10$, consistent with the correct asymptotic variation of the sub-grid length scale with the distance from the wall as enforced by the dynamic Smagorinsky model. LES under-predicts the peak value of normal stresses, also consistent with the predictions of LES based on finite difference methods. Since the multidomain method is not dissipative, the under-prediction is attributed to the under-dissipative nature of the dynamic model.

The LES methodology was shown to be robust, i.e. it is able to predict high-Reynolds-number flows with fair accuracy on a relatively coarse grid. Robustness was demonstrated by a simulation of the channel flow at $Re = 10\,000$. The mean flow and the Reynolds stress are in fair agreement with the published DNS result. The dynamic model is known to under-predict the sub-grid shear stresses in turbulent channel flows, especially at high Reynolds numbers. This leads to the error in the prediction of averaged velocity unless the resolution is increased sufficiently to reduce the proportion of the shear stress carried by the model. The marginal resolution in our simulation results in under-prediction of the average velocity in the outer layer at $z^+ > 10$ and larger deviation of the Reynolds stresses compared with the low-Reynolds-number case.

With tests on the isotropic turbulence and the turbulent channel flow, the characteristics of the LES methodology have been exposed. Further research is currently under way to apply the methodologies presented here, for simulation of more complex flows such as the flow over a backward-facing step. Complex flow elements including upstream boundary layer development,

DOI: 10.1002/fld

separation at the step, unstable curved shear layer, turbulent reattachment, and turbulent flow recovery make the flow a challenging case for our LES methodology.

The multidomain spectral method is of the same type as the discontinuous Galerkin method and the discontinuous finite element method. The conclusion and observations from this paper thus extend to this broader class of numerical methods.

ACKNOWLEDGEMENTS

The support for this study was provided by the U.S. Office of Naval Research with Dr G. D. Roy as the Program Officer. Computational time was provided in part by National Center for Supercomputing Applications (NCSA).

REFERENCES

1. Ghosal S. An analysis of numerical errors in large-eddy simulations of turbulence. *Journal of Computational Physics* 1996; **125**:187–206.
2. Kravchenko AG, Moin P. On the effect of numerical errors in large eddy simulation of turbulent flows. *Journal of Computational Physics* 1997; **131**:310–322.
3. Bui TT. A parallel, finite volume algorithm for large-eddy simulation of turbulent flows. *Computers and Fluids* 2000; **29**:877–915.
4. Mahesh K, Constantinescu G, Moin P. A numerical method for large-eddy simulation in complex geometries. *Journal of Computational Physics* 2004; **197**:215–240.
5. Jansen K. A stabilized finite element method for computing turbulence. *Computer Methods in Applied Mechanics and Engineering* 1999; **174**:299–317.
6. Santhanam S, Lele SK, Ferziger JH. A robust high-order compact method for large-eddy simulation. *Journal of Computational Physics* 2003; **191**:392–419.
7. Blaisdell GA, Spyropoulos ET, Qin JH. The effect of the formulation of nonlinear terms on aliasing errors in spectral methods. *Applied Numerical Mathematics* 1996; **21**:207.
8. Moin P, Squires K, Cabot W, Lee S. A dynamic subgrid model for compressible turbulence and scalar transport. *Physics of Fluids A* 1991; **3**(11):2746–2757.
9. Karniadakis GEM, Sherwin S. *Spectral/hp Element Methods for Computational Fluid Dynamics*. Oxford University Press: New York, U.S.A., 2005.
10. Deville MO, Fischer PF, Mund EH. *High-order Methods for Incompressible Fluid Flow*. Cambridge University Press: Cambridge, U.K., 2002.
11. Blackburn HM, Schmidt S. Spectral element filtering techniques for large eddy simulation with dynamic estimation. *Journal of Computational Physics* 2003; **186**:610–629.
12. Fischer PF, Mullen JS. Filter based stabilization of spectral element methods. *Comptes Rendus de l'Academie des Sciences Paris*, *Serie 1*, *Analyse Numerique* 2001; **332**:265–270.
13. Levin JG, Iskandarani M, Haidvogel DB. A spectral filtering procedure for eddy-resolving simulations with a spectral element ocean model. *Journal of Computational Physics* 1997; **137**:130–154.
14. Karamanos GS. Large eddy simulation using unstructured spectral/*hp* finite elements. *Ph.D. Thesis*, Imperial College, London, 1999.
15. Karamanos GS, Karniadakis GE. A spectral vanishing viscosity method for large-eddy simulations. *Journal of Computational Physics* 2000; **163**:22–50.
16. Jacobs GB, Kopriva DA, Mashayek F. Validation study of a multidomain spectral code for simulation of turbulent flows. *AIAA Journal* 2005; **43**(6):1256–1264.
17. Kopriva DA, Kolias JH. A conservative staggered-grid Chebyshev multidomain method for compressible flows. *Journal of Computational Physics* 1996; **125**:244–261.
18. Kopriva DA. A staggered-grid multidomain spectral method for compressible Navier–Stokes equations. *Journal of Computational Physics* 1998; **143**:125–158.
19. Jacobs GB. Numerical simulation of two-phase turbulent compressible flows with a multidomain spectral method. *Ph.D. Thesis*, University of Illinois at Chicago, Chicago, 2003.

DOI: 10.1002/fld

20. Salman H, Hesthaven JS, Warburton T, Haller G. Predicting transport by Lagrangian coherent structures with a high-order method. *Theoretical and Computational Fluid Dynamics* 2007; **21**:39–58.
21. Diamessis PJ, Domaradzki JA, Hesthaven JS. A spectral multidomain penalty method model for the simulation of high Reynolds number localized incompressible stratified turbulence. *Journal of Computational Physics* 2005; **202**:298–322.
22. Bassi F, Rebay S. A high-order accurate discontinuous finite element method for the numerical solution of compressible Navier–Stokes equations. *Journal of Computational Physics* 1997; **131**:267–279.
23. Collis SS. Resolution requirements in large-eddy simulation of shear flows. *Proceedings of the Summer Program*. Center for Turbulence Research, Stanford University: Stanford, CA, 2002.
24. Vreman B, Guerts B, Kuerten H. Subgrid-modeling in LES of compressible flow. *Applied Scientific Research* 1995; **54**:191–203.
25. Vreman B, Guerts B, Kuerten H. Large-eddy simulation of turbulent mixing layers. *Journal of Fluid Mechanics* 1997; **339**:357–390.
26. Germano M, Piomelli U, Moin P, Cabot WH. A dynamic subgrid scale eddy viscosity model. *Physics of Fluids A* 1991; **3**(7):1760–1765.
27. Yoshizawa A. Statistical theory for compressible turbulent shear flows, with the application to subgrid modeling. *Physics of Fluids A* 1986; **29**(7):2152–2164.
28. Erlebacher G, Hussaini MY, Speziale CG, Zang TA. Toward the large-eddy simulation of compressible turbulent flows. *Journal of Fluid Mechanics* 1992; **238**:155–185.
29. Squires KD. Dynamic subgrid scale modeling of compressible turbulence. *Annual Research Brief*, Stanford University, 1991.
30. Vreman AW, Guerts BJ, Kuerten J. *Direct and Large-eddy Simulation*, vol. I. Kluwer Academic Publishers: Netherlands, 1994.
31. Okong'o N, Knight DD, Zhou G. Large-eddy simulations using an unstructured grid compressible Navier–Stokes algorithm. *International Journal of Computational Fluid Dynamics* 2000; **13**(4):303–326.
32. Lily DK. A proposed modification of the Germano subgrid-scale closure method. *Physics of Fluids A* 1992; **4**(3):633–635.
33. Bardina J, Ferziger JH, Reynolds WC. Improved turbulence models based on large eddy simulation of homogeneous, incompressible, turbulent flows. *Report*, Thermosciences Division, Department of Mechanical Engineering TF-19, Stanford University, 1983.
34. Rogallo RS. Numerical experiments in homogeneous turbulence. *NASA Report TM 81315*, NASA, 1981.
35. Blaisdell GA, Mansour NN, Reynolds WC. Compressibility effects on the growth and structure of homogeneous turbulent shear flow. *Journal of Fluid Mechanics* 1993; **256**:443–485.
36. Smits AJ, Dussage JP. *Turbulent Shear Layers in Supersonic Flow*. Springer: Berlin, 2006.
37. Domaradzki JA, Loh KC, Yee PP. Large eddy simulations using the sub-grid scale estimation model and truncated Navier–Stokes dynamics. *Theoretical and Computational Fluid Dynamics* 2002; **15**(6):421–450.
38. Mathew J, Lechner R, Foysi H, Sesterhenn J, Friedrich R. An explicit filtering method for large-eddy simulation of compressible flows. *Physics of Fluids* 2003; **15**:2279–2289.
39. Bogey C, Bailly C. Computation of a high Reynolds number jet and its radiated noise using large eddy simulation based explicit filtering. *Computers and Fluids* 2006; **35**:1344–1358.
40. Piomelli U. Large-eddy simulation: achievements and challenges. *Progress in Aerospace Sciences* 1999; **35**: 335–362.
41. Moin P, Kim J. Numerical investigation of turbulent channel flow. *Journal of Fluid Mechanics* 1982; **118**:341–377.
42. Piomelli U. High Reynolds number calculations using the dynamic subgrid-scale stress model. *Physics of Fluids A* 1993; **5**(6):1484–1490.
43. Wang WP, Pletcher RH. On the large eddy simulation of a turbulent channel flow with significant heat transfer. *Physics of Fluids* 1996; **8**(12):3354–3366.
44. Lenormand E, Sagaut P, Ta Phuoc T. Large eddy simulation of subsonic and supersonic channel flow at moderate Reynolds number. *International Journal for Numerical Methods in Fluids* 2000; **32**:369–406.
45. Jacobs GB, Kopriva DA, Mashayek F. A conservative isothermal wall boundary condition for the compressible Navier–Stokes equation. *Journal of Scientific Computing* 2007; **30**(2):177–192.
46. Ridder JP, Beddini R. Large eddy simulation of compressible channel flow. *NASA Technical Report NGT-50363*, NASA, 1993.
47. Moser R, Kim J, Mansour NN. Direct numerical simulation of turbulent channel flow up to $Re_\tau = 590$. *Physics of Fluids* 1999; **11**(4):943–945.

DOI: 10.1002/fld

48. Niederschulte MA, Adrian RJ, Hanratty TJ. Measurements of turbulent flow in a channel at low Reynolds numbers. *Experiments in Fluids* 1990; **9**:222–230.
49. Ghosal S, Moin P. The basic equations for the large-eddy simulation of turbulent flows in complex geometry. *Journal of Computational Physics* 1995; **118**:24–37.
50. Zhao H, Voke PR. A dynamic subgrid-scale model for low-Reynolds number channel flow. *International Journal for Numerical Methods in Fluids* 1996; **23**:19–27.
51. Bagget JS, Jimenéz J, Kravchenko AG. Resolution requirements in large-eddy simulation of shear flows. *Annual Research Briefs*, Center for Turbulence Research, Stanford University, Stanford, CA, 1997.
52. Jimenéz J, Moser RD. Large-eddy simulations: where are we and what can we expect? *AIAA Journal* 2000; **38**(4):605–612.
53. Najjar FM, Tafti DK. Study of discrete test filter and finite difference approximations for the dynamic subgrid-scale stress model. *Physics of Fluids* 1996; **8**(4):1076–1088.

DOI: 10.1002/fld